Title

Momentum-resolved resonant inelastic soft X-ray scattering (qRIXS) endstation at the ALS

Authors

Chuang, YD
Feng, X
Cruz, A
et al.

Publication Date

2022-05-01

DOI

10.1016/j.elspec.2019.146897

Peer reviewed

Momentum-Resolved Resonant Inelastic Soft X-Ray Scattering (qRIXS) Endstation at the ALS

Yi-De Chuang,[1, a)] Xuefei Feng,[1] Alejandro Cruz,[1] Kelly Hanzel,[2] Adam Brown,[2] Adrian Sprucce,[2] Alex Frano,[1, 3] Wei-Sheng Lee,[4] Jaemyung Kim,[1] Yu-Jen Chen,[1] Brian Smith,[2] John S. Pepper,[2] Yu-Cheng Shao,[1, 5] Shih-Wen Huang,[6] L. Andrew Wray,[7] E. Gullikson,[8] Zhi-Xun Shen,[4, 9] Thomas Devereaux,[4] Anton Tremsin,[10] Wanli Yang,[1] Jinghua Guo,[1] Robert Duarte,[2] and Zahid Hussain[1]

[1)] *Advanced Light Source, Lawrence Berkeley National Laboratory, Berkeley, California 94720, USA*

[2)] *Engineering Division, Lawrence Berkeley National Laboratory, Berkeley, California 94720, USA*

[3)] *Department of Physics, University of California San Diego, La Jolla, California 92093, USA*

[4)] *Stanford Institute for Materials and Energy Sciences, SLAC National Accelerator Laboratory, Menlo Park, California 94025, USA*

[5)] *Department of Physics, Tamkang University, New Taipei City 25137, Taiwan, R.O.C.*

[6)] *MAX IV Laboratory, Lund University, PO Box 118, 22100, Lund, Sweden*

[7)] *Department of Physics, New York University, New York, New York 10003, USA*

[8)] *Center for X-Ray Optics, Lawrence Berkeley National Laboratory, Berkeley, California 94720, USA*

[9)] *Department of Physics, Stanford University, Stanford, California 94305, USA*

[10)] *Space Science Laboratory, University of California, Berkeley, California 94720, USA*

(Dated: 17 April 2019)

An endstation designed to operate at different beamlines at synchrotron and Free Electron Laser (FEL) facilities is presented. This enstation (qRIXS), currently located at the Advanced Light Source (ALS), has five emission ports on the experimental chamber for mounting the high-throughput modular soft X-ray spectrometers (MXS). Coupled to the rotation from the supporting hexapod, the scattered X-rays from 27.5° (forward scattering) to 152.5° (backward scattering) relative to the incident photon beam can be recorded, enabling the momentum-resolved RIXS spectroscopy. The components of this endstation are described in details, and the preliminary RIXS measurements on highly oriented pyrolytic graphite (HOPG) reveal the low energy vibronic excitations from strong electron-phonon coupling at C K edge around σ^* band. The grating upgrade option to enhance the performance at low photon energies is presented, and the potential of this spectroscopy is discussed in summary.

I. INTRODUCTION:

With advanced grating fabrication technology and the ability to tightly focus the intense soft X-ray beam from 3rd generation synchrotron storage ring down to few μm in size, grating-based soft X-ray spectrometers (referred to as spectrometers hereafter) can be designed to achieve unprecedented resolving power and/or throughput to meet different scientific demands. For example, spectrometers can be designed to have high or ultra-high resolving power with pre-mirror(s) to increase the collection angle,[1–5] or achieve high throughput with compact form factor,[6–10] or utilize multiple diffraction orders of grating simultaneously to record spectra over a wide energy window,[11] or take advantage of the off-axis radiation usually blocked out by beamline exit slit with energy compensation[12] and cross-dispersion[13] optical schemes. Using these spectrometers, the potential of resonant inelastic soft X-ray scattering spectroscopy (RIXS) has been demonstrated in studying the electronic structures of correlated, functional, and energy materials under UHV and *in-situ*/*operando* conditions.[14–18]

In RIXS process, the incident photons with energy $\hbar\omega$ tuned to elemental absorption edge resonantly excite core electrons to unoccupied states followed by the re-emission of photons with energy $\hbar\omega'$ when core holes are filled. The difference between energy (ΔE=$\hbar\omega$-$\hbar\omega'$) and momentum ($\Delta\vec{q}$=$\vec{k}$-$\vec{k}'$) of incident and emitted photons is then transferred to elementary excitations such as phonons, magnons, orbital excitations, charge transfer excitations, ... etc., that are unique to the materials under study. The ability to directly obtain the dispersion of these excitations makes RIXS a powerful technique that complements other single-particle spectroscopies such as angle-resolved photoemission spectroscopy (ARPES).[18–23]

In order to exploit this potential, the RIXS instrument needs to record X-rays emitted from sample at different angles relative to the incident X-ray beam, i.e. varying

[a)] Correspondence should be addressed to ychuang@lbl.gov

$\vec{k}'$ relative to $\vec{k}$, and judiciously project the momentum transfer $\Delta\vec{q}$ along certain momentum space trajectory [typically along the crystalline high symmetry cuts]. In fact, the RIXS spectral intensity contains far richer information about the underlying quantum wave functions, as this can be perceived from its differential cross-section in Kramers-Heisenberg formalism:

$$\left.\frac{d^2\sigma}{d\Omega_{k'}d(\hbar\omega')}\right|_{g\to f} \propto$$

$$\frac{\omega'}{\omega}\left|\sum_n \frac{\langle f|T_o^\dagger|n\rangle\langle n|T_i|g\rangle}{E_g - E_n + \hbar\omega + i\Gamma/2}\right|^2 \times \delta(E_g - E_f + \Delta E)$$

Here $|g\rangle$, $|n\rangle$, and $|f\rangle$ denote the ground, intermediate, and final states. E_n is the energy of intermediate state and Γ is the lifetime. $T_{i(o)}$ is the transition operator that depends on incident (emitted) photon polarization $\hat{\epsilon}_{i(o)}$ and electron momentum $\vec{p}$:

$$T_{i(o)} = [\vec{p}\cdot\hat{\epsilon}_{i(o)}]e^{i\vec{k}^{(\prime)}\cdot\vec{x}}$$

From this dependence, one sees that RIXS spectral intensity will be influenced by the projection of photon momentum $\vec{k}$ and $\vec{k}'$, not just only $\Delta\vec{q}$, with respect to ground and final state wave functions.

This notion, well-received by RIXS community, drives the design of RIXS instruments to have maximum flexibility: six degrees of freedom for sample manipulation and the ability to rotate spectrometer(s) relative to the incident X-ray beam in the scattering plane. For soft X-ray applications, the challenge lies in maintaining high vacuum for both experimental chamber and spectrometer(s) while being able to rotate the spectrometer(s). Novel solutions for vacuum interface, such as using the sliding face seal[4] or multiple rotary stages[5], often lead to endstation designs that are unique to the respective beamline designs. To develop an endstation that can be used at different beamlines and facilities as required by this project, we have taken a different approach: the spectrometer is designed to be modular and can be moved to different emission ports on the experimental chamber. By rotating the entire endstation, the emission angles of X-rays from 27.5° (forward scattering) to 152.5° (backward scattering) relative to the incident beam (defined as 0°) can be continuously covered. The CAD model of this momentum-resolved RIXS endstation (qRIXS) in shown Figure 1.

This paper describes the design of qRIXS at BL8.0.1 of the Advanced Light Source (ALS), Lawrence Berkeley National Laboratory. The modular soft X-ray spectrometer (MXS) was described in previous publication and will not be discussed in details except its proposed upgrade.[24] The paper is structured as follows: in Section II, we present the mechanical design of endstation components. In Section III, we show the preliminary results of the electronic structures of highly oriented pyrolytic graphite (HOPG) using MXS with Timepix detector to reveal phonon overtones.[25] In Section IV, we present the optical design of a new blazed grating that will be installed in MXS to enhance its performance at low photon energies. In Section V, we give the summary and outlook of applications for momentum-resolved RIXS spectroscopy.

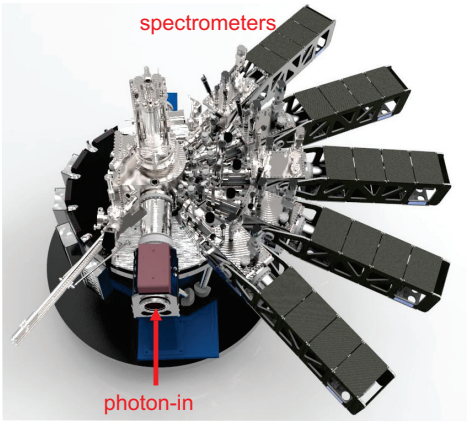

FIG. 1. CAD model of qRIXS with five modular soft X-ray spectrometers (MXS) mounted on top of the experimental platform.

II. MECHANICAL DESIGN OF MOMENTUM RESOLVED RIXS ENDSTATION (QRIXS):

The endstation consists of the following major components: sample manipulation, detectors, experimental chamber and support, loadlock chamber, vacuum and motion control. Each component will be described in the following subsections.

A. Sample Manipulation

The sample manipulation is nearly identical to that of RSXS endstation reported earlier.[26] The open cycle cryostat and sample goniometer are fabricated at the ALS (see Figure 2(a) for the picture of sample goniometer). There are two rotational degrees of freedom on sample goniometer: about the sample surface normal (ϕ) and virtual-axis vertical flip downward (χ). They have 360° (±180°) and 75° (+10° ∼ -65°) range of rotation, respectively. These motions are driven by motorized rotary feedthroughs (IMS MDI3CRL23B7-EE motors) with 0.1° step resolution. The goniometer is isolated from cryostat cold finger via a sapphire disk to allow the total electron yield measurement (TEY, measuring the sample-to-ground drain current). A radiation shield partially wraps around the goniometer to reduce the radiative heating. A cartridge heater attached to the cold finger is used to control sample temperature from ∼ 13 K up to 450 K, where the high temperature limit is set by the Lakeshore

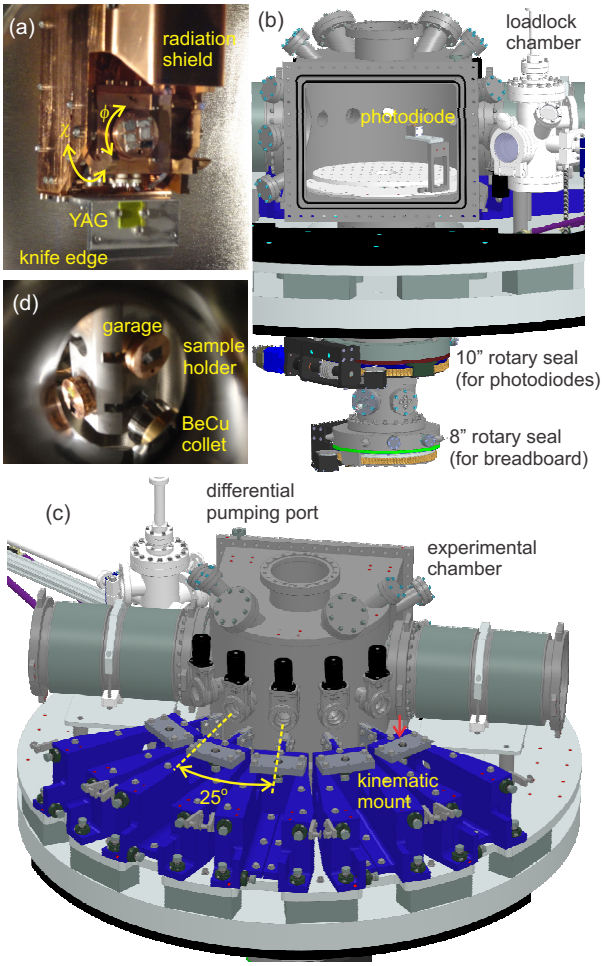

FIG. 2. (a) Picture of cryostat showing the rotational degrees of freedom ϕ and χ. The YAG and knife edge are mounted below the goniometer. (b) CAD model showing the rectangular flange, photodiode assembly, and two rotary seals. (c) CAD model showing the five emission ports on the half-circular side of experimental chamber. The angular separation between ports is 25°. The red arrow marks the 1/2-20 screw on the kinematic mounting assembly for adjusting the spectrometer pitch angle. (d) Picture of sample garage, BeCu sample grabber, and sample holders inside loadlock chamber.

DT-670 diodes. A 10 mm×10 mm YAG crystal and a knife-edge are mounted below the goniometer for viewing X-ray beam and measuring its vertical size. A 2" OD support tube clamped on the cold finger and attached to the vacuum side of top 6" flange provides additional rigidity for the cryostat, and a hydraulic formed bellow connecting the top of cryostat assembly to the air side of 6" flange helps reduce sample movement during temperature cycles.

The cryostat assembly is mounted on a motorized VG Omniax manipulator (IMS MDI3CRL23B7-EE motors for in-plane x and y motions, and MDI3CRL34B7-EE motor for vertical z motion), providing the three translational degrees of freedom. This manipulator has ±25 mm and 200 mm travel range for horizontal and vertical motions, respectively. These motions are encoded by optical encoders with 0.1 μm step resolution (Renishaw RGH24Y-50F-33A). The manipulator is placed on top of an 8" differentially pumped rotary seal (Nor-Cal RS-600, driven by MDI3CRL34B7-EE motor), which rotates the sample 360° in the horizontal plane (θ). The motor stepping provides the step resolution better than 0.01°.

B. Detectors

Besides spectrometers, there are two GaAsP photodiodes (Hamamatsu G1127-04) mounted inside their respective housing for detecting photons. One of the photodiodes has a 150 nm thick Al window (supported by a 70 lines/inch Ni mesh with 84% transmission) attached to the front face of its housing to block out ambient visible light and photoelectrons emitted from sample. The backside of housing is packed with graphite-coated Cu wool to form a black box, minimizing the leakage light through the venting hole while allowing the gas inside the housing to be pumped out. The photodiode signal is transmitted through Kapton-coated 50 Ω impedance matching coaxial cables (MDC CAP-5) to SMA feedthroughs on the chamber. The current signal is then converted by the low noise current amplifier (Femto DDPCA-300) to DC voltage.

The photodiodes are mounted on a rotary platform driven by a motorized 10" rotary seal (MDI3CRL23B7-EE motor with Parker PX23-030-S2 30:1 gearbox) below the experimental chamber. In addition, there is a breadboard with an array of 1/4-20 tapped holes for mounting auxiliary equipments, such as refocusing mirrors for pump beams, electromagnets, pinholes, ... etc., to expand the experimental capability. The breadboard sits slightly above the photodiode mounting brackets and is driven by another motorized 8" rotary seal using the same model of motor and gearbox. The rotary seals are concentric to each other, see Figure 2(b) for CAD model. The arrangement of three differential rotary seals allows the sample, photodiodes, and breadboard to be rotated independently. Since the angular acceptance angle of photodiode is large (∼ 2.5°), the high degree of concentricity for these three rotary stages is not required.

C. Experimental Chamber and Support

The aspect view of experimental chamber is shown in Figure 2(c). The chamber has half-circular shape [diameter is 17.75"] with symmetric port arrangement to allow the photon beam to come from either direction. There are five 2-3/4" emission ports on the circular side of chamber at 40° (forward direction), 65°, 90°, 115°, and 140° (backward direction) angle relative to the 10" beam entry bellows. Coupled to the 25° chamber rotation from the supporting hexapod (see later discussion), the

emission angle of X-rays from 27.5° to 152.5° relative to the incident beam can be covered. The emission ports have manual gate valves on them (VAT 01032-UE01-0002), and MXS has a 4-1/2" manual gate valve with a 1.33" pump out port in front of optics chamber (VAT 10836-UE01-AEN1). By closing these two valves and venting/pumping through the pump out port, both experimental chamber and MXS can stay in vacuum when removing and connecting the bellow in between them. Below these emission ports, there are ribs welded to the chamber wall for attaching the spectrometer kinematic support assembly. The assembly consists of multiple Al blocks and six kinematic pads for reproducibly positioning the spectrometer (repeatability better than 25 μm; with spherical and flat carbide contact faces on MXS and kinematic assembly). The most critical one, pitching the spectrometer vertically to change the incidence angle, can be adjusted by the 1/2-20 screw on the top plate (see red arrow in Figure 2(c)).

The chamber has a rectangular door on the opposing side for accessing the interior (see Figure 2(b)). The door is currently sealed with double O-rings and the space in between O-rings is kept at rough vacuum through differential pumping. The rectangular flange and the door have ground surfaces for using Al wire seal for UHV applications, if needed. A large turbo pump (Agilent V551) mounted on the door and backed by molecular drag pump (Adixen Alcatel Drytel 1025) pumps the chamber down to a base pressure better than 2×10^{-8} torr. Two bellows are used to connect the experimental chamber to upstream refocus mirror chamber and downstream beam pipe to balance the vacuum forces. To allow the 25° chamber rotation, the bellows are sized to go with 10" flanges and with sufficient length to reach such extreme angle (±12.5°) for more than 10,000 duty cycles. The chamber is placed on top of a 1" thick Al plates with more than 150 lb counter weight on it. This top plate is secured to another 3" thick Al bottom plate with 24 spacer blocks in between them. A large slewing ring bearing (Kaydon KH-166P) is placed in between these two plates in case if the rotational range needs to be increased for future applications.

The endstation assembly is placed on top of a motorized hexapod (Symetrie Joran series). With 8300 lb payload and 1860 N shearing forces applied on the opposing sides of platform to simulate the bellow forces at 12.5° extreme angle, the hexapod was tested to achieve the translational and rotational step size of 1 μm and 5 μrad with repeatability of 2.8 μm and 2 μrad, respectively. The actuators in hexapod have absolute encoders to keep track of their positions in case of power failure. A virtual rotational axis is defined through hexapod software so that during the hexapod rotation, the sample runout relative to the photon beam is $\sim$ 100 μm, which is smaller than the depth of focus of MXS.

D. Loadlock Chamber

A dedicated loadlock chamber is used to introduce samples from air into experimental chamber without venting it (see Figure 2(b)). It has a garage for holding up to 12 sample holders, see picture in Figure 2(d). A dual action magnetic transfer arm is used to actuate the Beryllium Copper collet against the phosphor bronze block to grab and release the sample holder. A viewport door (MDC P/N 665206) is used to allow the easy access for loading and retrieving sample holders from loadlock chamber. The chamber is pumped by a small turbo pump (Agilent V81) backed a scroll pump (Agilent SH-110) to reach $\sim 2\times10^{-8}$ torr base pressure.

E. Vacuum Monitoring and Motion Control

To avoid visible light from vacuum gauges that can influence the photon detectors like CCD and GaAsP photodiode, we have used cold cathode gauges in both experimental and loadlock chambers (MKS Imag 423 with MKS 937 gauge controller) to monitor the vacuum level. The vacuum gauge readings are routed to the process logic control (PLC) computer in the beamline for equipment protection in case of vacuum breach.

Since the IMS motors have onboard controllers, the control protocol is sent through ethernet based port servers (Digi TS16 MEI) from computer to motors. A dedicated electronic board, designed and fabricated by SLAC National Accelerator Laboratory to distribute the 75 V DC to power the motor, optical encoder (12 V), and limit switches (5 V), is used for protecting the motors from back EMF and allowing the hot-swapping.

III. PRELIMINARY RIXS MEASUREMENTS ON HOPG

Here we show the results of RIXS measurements on HOPG in Figure 3. More details will be reported elsewhere. Commercial HOPG sample (SPI supplies) was mounted on the sample holder using carbon tape and was cleaved in air before introducing into the loadlock chamber. The sample was oriented with Γ-M roughly in the horizontal scattering plane with incident photon polarization (π scattering geometry; sample mosaicity of $\sim \pm5°$ was found in Laue pattern). In Figure 3(a), we show the room temperature RIXS spectrum recorded using iRIXS endstation with MXS at 90° relative to incident photon beam.[27,28] The excitation photon energy was 291.8 eV, at the peak of σ^* band in the X-ray absorption spectrum (XAS, see arrow in the inset of Figure 3(a)). The sample was placed at $\sim$ 45° incidence angle. At such geometry, the elastic peak becomes the dominant feature in the spectrum, stronger than the interband transition features in the [10 eV, 25 eV] energy loss window.

However, zooming in the region around the elastic peak (zero energy loss, see top panel in Figure 3(b)) reveals

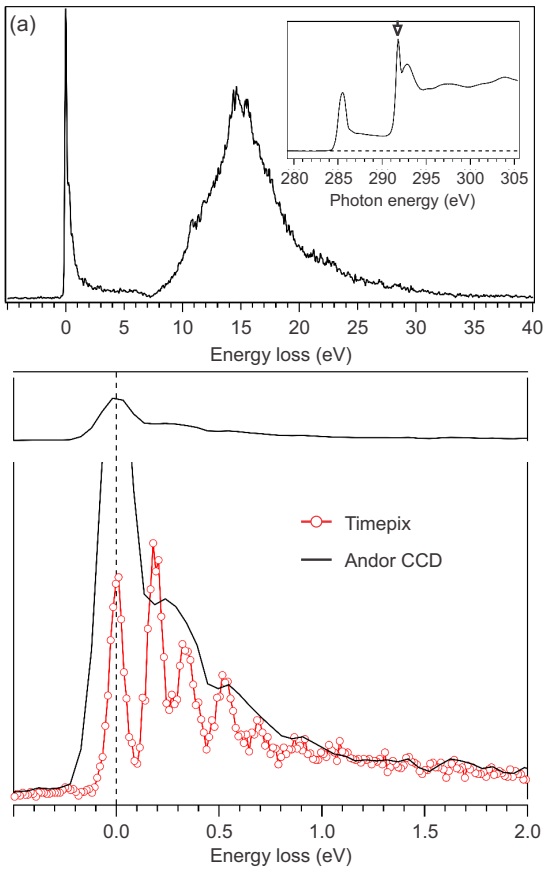

FIG. 3. (a) RIXS spectrum of HOPG taken at 291.8 eV incident photon energy around σ^* band using a commercial CCD detector (Andor iKon CCD). This energy is marked by an arrow in the XAS spectrum in the inset. (b) Zoomed in view of RIXS spectrum around the elastic peak (top panel; [-0.5 eV, 2 eV] energy loss window) and the comparison of RIXS spectra taken with Andor CCD (thin black line) and Timepix detector (red open circles and line) showing the improved energy resolution to resolve phonon overtones (bottom panel).

weak features as reported previously using MXS with SpectroCCD detector.[28] These features are phonon overtones induced by the configuration change during RIXS process. However, the poor pixel resolution of Andor CCD detector leads to much broader humps around energy loss of 0.3, 0.6, and 0.9 eV as shown in the bottom panel of Figure 3(b). Although the 5 μm pixel resolution from SpectroCCD detector helps resolve these phonon overtones, the strong elastic peak still plagues these modes such that they all sit on top of a sloping background from the tail of elastic peak.[28]

We repeat the same measurement using MXS with Timepix detector at qRIXS endstation. The Timepix detector with 6 μm MCP pores has been shown to achieve an effective pixel resolution of 7.5 μm after using centroiding algorithm. We vary the sample and MXS angles to suppress the elastic peak while keeping it strong enough to register the zero energy loss. By placing MXS at 102.5° and sample normal at 36.5° relative to the incident photon beam (slightly off spectular geometry), the resulting RIXS spectrum with significantly reduced elastic peak is shown in the bottom panel of Figure 3(b) (red open circles). To achieve high energy resolution, the beamline slits were set to 20 μm × 20 μm, and the combined energy resolution determined from the FWHM of elastic peak is ∼ 70 meV. With such energy resolution and the much weaker elastic peak, the phonon overtones can be clearly resolved.

IV. DESIGN OF NEW BLAZED GRATING

A. Optical Design

From previous section, we see that even with a combined energy resolution of ∼ 70 meV around C K-edge, it is still sufficient to resolve phonon overtones in HOPG. Therefore, we expect that qRIXS and iRIXS endstations equipped with several MXS can be used to study electronic structures of carbon-based materials. However, the overall throughput is rather low: the high resolution spectrum in Figure 3(b) takes about 4 hours to record. This is largely due to the small beamline entrance and exit slit setting needed to improve energy resolution, as well as lower grating and detector efficiencies at this energy range. The Timepix detector used in the measurement has a chevron angle not optimized for current application and did not have photocathode coating (like CsI or KBr) at that time. In addition, the grating has relatively low efficiency due to laminar profile (see Figure 4(f)).

With the availability of blazed grating, we now look into the design of a new grating that will be blazed for high 1st and 2nd order diffraction efficiencies to replace the exist one. To minimize the engineering effort, the upgrade only requires swapping out the current grating inside optics chamber without any modification on mechanical components. Furthermore, the new grating shall have comparable or even higher 2nd order efficiency than the current one such that there is minimal loss on high energy performance. With these considerations, we vary the central line density and grating incidence angle α, and design it to work with 20 μm source size (the beam size is slightly smaller than 20 μm) and 7 μm detector pixel resolution.

The following parameters are used in optical design: r_{SM}=0.9 m, r_{MG}=0.1 m, and r_{GD} ∼ 1.1 m (this distance will depend on photon energy), R=29.472 m, θ=88°, and α=88.2° (changed from 88.5°). Here, r_{SM}, r_{MG}, r_{GD} are the sample-to-mirror, mirror-to-grating, and grating-to-detector distances. R is the radius of spherical mirror and θ is its incidence angle. The grating will be operated in inside order at nearly constant incidence angle. α can be slightly changed to minimize the vector sum of coma F_{30} and spherical aberration F_{40} terms, see later discussion. The maximum vertical acceptance angle of spectrometer

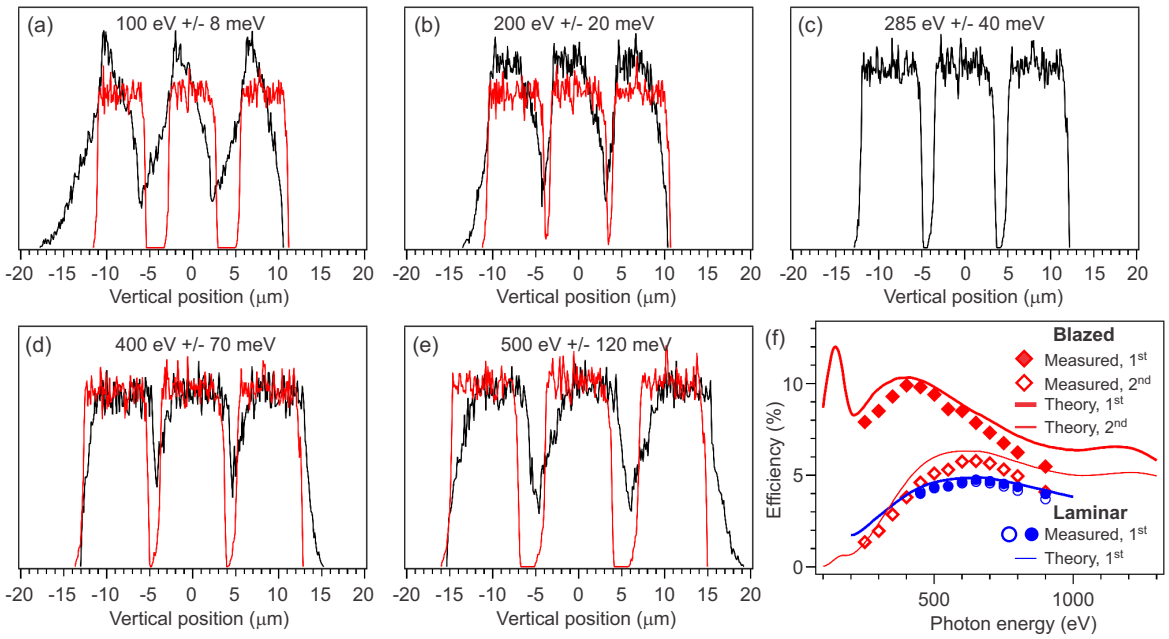

FIG. 4. (a)-(e) SHADOW simulations showing the histograms at the detector plane at selected photon energies: (a) 100 eV, (b) 200 eV, (c) 285 eV, (d) 400 eV, and (e) 500 eV. The red and black curves are the results with and without optimizing α and r_{GD} to minimize the vector sum of F_{30} and F_{40}. (f) Efficiency curves of the gratings. The thick and thin red lines are the calculated 1st and 2nd order efficiencies with blaze profile, and the filled and open diamonds are the measured 1st and 2nd order efficiencies from test sample. The thin blue line is the 1st order efficiency with laminar profile. The markers are the measured efficiency for current grating.[24]

is increased from 2.6 mrad to 3.0 mrad due to the smaller α angle, and the horizontal acceptance angle remains at 60 mrad. We follow the approach by Amemiya *et al.*[29,30] to determine the VLS terms at 285 eV. The calculated VLS terms g_0 (constant), g_1 (linear), g_2 (quadratic), and g_3 (cubic) are (in SHADOW convention[31,32]): g_0=15,000 lines/cm, g_1=272.139 lines/cm^2, g_2=3.577 lines/cm^3, and g_3=0.0444 lines/cm^4. The local groove density $g(\omega)$ can be calculated as follows: $g(\omega) = g_0 + g_1 \times \omega + g_2 \times \omega^2 + g_3 \times \omega^3$, where ω is the signed tangential distance on the grating surface from grating pole. Positive ω points to the downstream direction.

B. SHADOW Ray-Tracing Results and Grating Efficiency

Figures 4(a) - 4(e) show the SHADOW ray-tracing results with aforementioned parameters at selected photon energies from 100 eV to 500 eV when grating is operated in 1st order [we expected to see similar performance at doubled photon energy when grating is operated in 2nd order]. In the simulations, the source is a 20 μm (v) $\times$ 100 μm (h) rectangle. The beam divergence is set to 3.0 mrad (v) $\times$ 100 μrad (h) to simplify the simulations and production of histograms from binning the detector images across the non-dispersive (horizontal) direction. The slope error contributions to energy resolution are negligible and are not included in simulations (RMS slope error of 0.3 μrad and 0.16μrad for spherical mirror and plane grating substrate, respectively). In each figure, there are three features representing X-rays with three different energies (one central and two detuned energies, which are listed on top of each panel) that are propagated through the optical system. The black and red curves are the results without and with the slight tuning of α (87.65° $\sim$ 88.48°) and r_{GD} (1092.5 mm $\sim$ 1102 mm).

From these figures, it is clear that the optimization procedure can significantly improve the image quality when photon energies are away from the 285 eV target energy, as expected. With improved image quality, the resolving power at 100 eV can exceed 10,000 if using the small pixel detectors (see Figure 4(a)). However, one should note that this claim does not take the Nyquist limit into consideration. The resolving power decreases with increasing photon energy. Due to increased central line density (effectively 30,000 lines/cm in 2nd order), the resolving power at 500 eV is slightly above 4,000 (see Figure 4(e)). If operated in 2nd order, this resolving power can be expected at 1,000 eV, which is higher than the designed value for the current grating in MXS.

The grating efficiency is calculated using GSolver® with Au coating. The thin blue line is the calculated 1st order efficiency for current grating with a laminar profile.[24] The blue filled and open circles are the measured efficiency for two rulings currently in MXS. The thick and thin red lines are the calculated blazed 1st and

2^{nd} order diffraction efficiency with the blaze and apex angles set to 2.2° and 165°, respectively. The red filled and open diamonds are the measured 1^{st} and 2^{nd} order efficiency of test sample from Inprentus Inc. Compared with current laminar grating, one can see that above ∼ 400 eV, the new grating will have comparable 2^{nd} order efficiency and much higher 1^{st} order efficiency up to 1,500 eV. What is intriguing is that at 285 eV, the blazed efficiency is almost 8%, 4 times higher than the current one. We notice that is discrepancy between the calculated and measured blazed efficiency curves and this is due to the larger apex angle than calculated, as well as the deviation from ideal blazed profile. Nevertheless, the overall performance of MXS in terms of energy resolution and efficiency will still be improved with this new grating in particular at low energies.

V. CONCLUSIONS AND OUTLOOK:

We have presented the design of a momentum-resolved RIXS endstation (qRIXS) at the ALS that currently has 3 modular soft X-ray spectrometers (MXS) on it. Using multiple emission ports on the experimental chamber and the 25° chamber rotation provided by the supporting hexapod, the emission angles of X-rays from 27.5° to 152.5° relative to the incident photon beam can be continuously covered. With ∼ 70 meV combined energy resolution from beamline and spectrometer and the small pixel Timepix detector (the effective pixel resolution is 7.5 μm after centroiding), we have clearly resolved the Frank-Condon like phonon overtones from σ^* bands in HOPG for the first time.[28] This measurement demonstrates the potential of using MXS and qRIXS for C-based research that is limited in most high-resolution RIXS facilities, and echoes the demand for high resolution RIXS spectroscopy even at low photon energies. With this consideration, we show the optical design of a new blazed VLS grating for the upgrade of MXS. With 2.2° blazed angle and 15,000 lines/cm central line density, the resolving power at 285 eV can be increased to 7,000 with ∼ 10% efficiency.

The potential of qRIXS will not be limited to measuring the low energy excitations in correlated materials. In fact, the very high detection efficiency of MXS that can record a good statistics spectrum in just one minute and the flexibility in manipulating sample and experimental geometry make qRIXS an ideal system for studying the incipient, fluctuating electronic orders ubiquitous to correlated materials with competing/cooperating ground states. One such example is the charge density wave (CDW) in cuprates.[33,34] Due to strong signal from inelastic excitations like magnons, orbital, and charge excitations, the pure elastic signal from fluctuating CDW will be severely masked when the X-ray signal is not energy-resolved. However, using the spectrometer to discriminate the elastic component from inelastic contributions, the CDW in cuprates can be unambiguously identified. We expect that similar approach can be used in other correlated materials besides cuprates that have intriguing ordering phenomena and phase transitions. For example, the colossal magnetoresistive manganites (Pr,Ca)MnO_3 with coupled charge, spin, and orbital orders around phase boundary,[35] the impurity-induced ordering in ruthenates,[36] or even the engineered heterostructure (RE)NiO_3, ... etc.[37,38] will be interesting topics to explore with qRIXS to elucidate the emergence of these electronic orderings from competing ground states. The qRIXS technique can also be extended to incorporate the standing wave concept, much like that used in standing wave photoemission, to explore interfacial dynamics.[39]

ACKNOWLEDGMENTS

The Advanced Light Source is supported by the Director, Office of Science, Office of Basic Energy Sciences, of the U.S. Department of Energy under Contract No. DE-AC02-05CH11231. SLAC National Accelerator Laboratory is supported by the U.S. Department of Energy, Office of Science, Office of Basic Energy Sciences under contract No. DE-AC02-76SF00515.

[1] G. Ghiringhelli, A. Piazzalunga, C. Dallera, G. Trezzi, L. Braicovich, T. Schmitt, N.V. Strocov, R. Betemps, L. Patthey, X. Wang, and M. Grioni, Rev. Sci. Instrum. **77**, 113108 (2006).
[2] N.V. Strocov, T. Schmitt, U. U. Flechsig, T. Schmidt, A. Imhof, Q. Chen, J. Raabe, R. Betemps, D. Zimoch, J. Krempasky, X. Wang, M. Grioni, A. Piazzalunga, and L. Patthey, J. Synchrotron Rad. **17**, 631 (2010).
[3] Y. Harada, M. Kobayashi, H. Niwa, Y. Senba, H. Ohashi, T. Tokushima, Y. Horikawa, S. Shin, and M. Oshima, Rev. Sci. Instrum. **83**, 013116 (2012).
[4] N.B. Brookes, F. Yakhou-Harris, K. Kummer, A. Fondacaro, J.C. Cezar, D. Betto, E. Velez-Fort, A. Amorese, G. Ghiringhelli, L. Braicovich, R. Barrett, G. Berruyer, F. Cianciosi, L. Eybert, P. Marion, P. van der Linden, L. Zhang, Nucl. Instrum. Methods Phys. Res. A **903**, 175 (2018).
[5] J. Dvorak, I. Jarrige, V. Bisogni, S. Coburn, and W. Leonhardt, submitted to Rev. Sci. Instrum. **87**, 115109 (2016).
[6] C. F. Hague, J. H. Underwood, A. Avila, R. Delaunay, H. Ringuenet, M. Marsi, and M. Sacchi, Rev. Sci. Instrum. **76**, 023110 (2005).
[7] Y.-D. Chuang, J. Pepper, W. McKinney, Z. Hussain, E. Gullikson, P. Batson, D. Qian, and M. Z. Hasan, J. Phys. Chem. Solids **66**, 2173 (2006).
[8] M. Agåker, J. Andersson, C.-J. Englund, A. Olsson, M. Ström, and J. Nordgren, Nucl. Instrum. Methods Phys. Res. A **601**, 213 (2009).
[9] S.G. Chiuzbăian, C.F. Hague, A. Avila, R. Delaunay, N. Jaouen, M. Sacchi, F. Polack, M. Thomasset, B. Lagarde, A. Nicolaou, S. Brignolo, C. Baumier, J. Lüning, and J.-M. Mariot, Rev. Sci. Instrum. **85**, 043108 (2014).
[10] Z. Yin, H.B. Peters, U. Hahn, M. Agåker, A. Hage, R. Reininger, F. Siewert, J. Nordgren, J. Viefhaus, and S. Techert, Rev. Sci. Instrum. **86**, 093109 (2015).
[11] O. Fuchs, L. Weinhardt, M. Blum, M. Weigand, E. Umbach, M. Bär, C. Heske, J. Denlinger, Y.-D. Chuang, W. McKinney, Z. Hussain, E. Gullikson, M. Jones, P. Batson, B. Nelles, and R. Follath, Rev. Sci. Instrum. **80**, 063103 (2009).
[12] C. H. Lai, H. S. Fung, W. B. Wu, H. Y. Huang, H. W. Fu, S. W. Lin, S. W. Huang, C. C. Chiu, D. J. Wang, L. J. Huang, T. C.

Tseng, S. C. Chung, C. T. Chen and D. J. Huang, J. Synchrotron Rad. **21**, 325 (2014).
[13]T. Warwick, Y.-D. Chuang, D.L. Voronov and H. Padmore, J. Synchrotron Rad. **21**, 736 (2014).
[14]Frank de Groot and Akio Kotani, *Core Level Spectroscopy of Solids*, CRC press, 2008.
[15]W. Yang, X. Liu, R. Qiao, P. Olalde-Velasco, J.D. Spear, L. Roseguo, J. Pepper, Y.-D. Chuang, J.D. Denlinger, and Z. Hussain, J. Electron. Spectrosc. Relat. Phenom. **190**, 64 (2013).
[16]X. Liu, W. Yang, and Z. Liu, Adv. Mater. **26**, 7710 (2014).
[17]Y.-S. Liu, P.-A. Glans, C.-H. Chuang, M. Kapilashrami, & J.-H. Guo, J. Electron. Spectrosc. Relat. Phenom. **200**, 282 (2015).
[18]L.J.P. Ament, M. van Veenendaal, T.P. Devereaux, J.P. Hill, and J. van den Brink, Rev. Mod. Phys. **83**, 705 (2011).
[19]J. Nordgren and J.-H. Guo, J. Electron. Spectrosc. Relat. Phenom. **110**, 1 (2000).
[20]A. Kotani and S. Shin, Rev. Mod. Phys. **73**, 203 (2001).
[21]W. Schülke, *Electron Dynamics by Inelastic X-Ray Scattering*, Oxford press, 2007.
[22]M. Simon and T. Schmitt, Editors, J. Electron. Spectrosc. Relat. Phenom. **188**, 1 (2013).
[23]T. Schmitt, F.M.F. de Groot, J.-E. Rubensson, J. Synchrotron Rad. **21**, 1065 (2014).
[24]Y.-D. Chuang, Y.-C. Shao, A. Cruz, K. Hanzel, A. Brown, A. Frano, R. Qiao, B. Smith, E. Domning, S.-W. Huang, L. A. Wray, W. S. Lee, Z.-X. Shen, T. P. Devereaux, J.-W. Chiou, W.-F. Pong, V. V. Yashchuk, E. Gullikson, R. Reininger, W. Yang, J. H. Guo, R. Duarte, and Z Hussain Rev. Sci. Instrum. **88**, 013110 (2017).
[25]A.S. Tremsin, J.V. Vallerga, J.B. McPhate, O.H.W. Siegmund, Nucl. Instrum. Methods Phys. Res., Sect. A **787**, 20 (2015).
[26]D. Doering, Y.-D. Chuang, N. Andresen, K. Chow, D. Contarato, C. Cummings, E. Domning, J. Joseph, J. S. Pepper, B. Smith, G. Zizka, C. Ford, W. S. Lee, M. Weaver, L. Patthey, J. Weizeorick, Z. Hussain, and P. Denes, Rev. Sci. Instrum. **82**, 073303 (2011).
[27]R. Qiao, Q. Li, Z. Zhuo, S. Sallis, O. Fuchs, M. Blum, L. Weinhardt, C. Heske, J. Pepper, M. Jones, A. Brown, A. Spucces, K. Chow, B. Smith, P.-A. Glans, Y. Chen, S. Yan, F Pan, L.F.J. Piper, J. Denlinger, J. Guo, Z. Hussain, Y.-D. Chuang, and W. Yang, Rev. Sci. Instrum. **88**, 033106 (2017).
[28]N.C. Andresen, P. Denes, A. Goldschmidt, J. Joseph, A. Karcher, and C.S. Tindall, Rev. Sci. Instrum. **88**, 083103 (2017).
[29]K. Amemiya, Y. Kitajima, T. Ohta, and K. Ito, J. Synchrotron Rad. **3**, 282 (1996).
[30]K. Amemiya and T. Ohta, J. Synchrotron Rad. **11**, 171 (2004).
[31]F. Cerrina and M. Sanchez del Rio, *Ray Tracing of X-Ray Optical Systems* Ch. 35 in Handbook of Optics (volume V, 3rd edition), edited by M. Bass, McGraw Hill, New York, 2009.
[32]M. Sanchez del Rio, N. Canestrari, F. Jiang and F. Cerrina, J. Synchrotron Rad. **18**, 708 (2011).
[33]G. Ghiringhelli, M. Le Tacon, M. Minola, S. Blanco-Canosa, C. Mazzoli, N. B. Brookes, G. M. De Luca, A. Frano, D. G. Hawthorn, F. He, T. Loew, M. Moretti Sala, D. C. Peets, M. Salluzzo, E. Schierle, R. Sutarto, G. A. Sawatzky, E. Weschke, B. Keimer, L. Braicovich, Science **337**, 821 (2012).
[34]H. Miao, J. Lorenzana, G. Seibold, Y. Y. Peng, A. Amorese, F. Yakhou-Harris, K. Kummer, N. B. Brookes, R. M. Konik, V. Thampy, G. D. Gu, G. Ghiringhelli, L. Braicovich, and M. P. M. Dean, PNAS **114**, 12430 (2017).
[35]T. Chatterji, *Colossal Magnetoresistive Manganites*, Kluwer Academic Publisher, 2004.
[36]M. A. Hossain, I. Zegkinoglou, Y.-D. Chuang, J. Geck, B. Bohnenbuck,, A. G. Cruz Gonzalez, H.-H. Wu, C. Schußler-Langeheine, D. G. Hawthorn, J. D. Denlinger, R. Mathieu, Y. Tokura, S. Satow, H. Takagi, Y. Yoshida, Z. Hussain, B. Keimer, G. A. Sawatzky, A. Damascelli, Sci. Rep. **3**, 2299 (2013).
[37]Jian Liu, Mehdi Kargarian, Mikhail Kareev, Ben Gray, Phil J. Ryan, Alejandro Cruz, Nadeem Tahir, Yi-De Chuang, Jinghua Guo, James M. Rondinelli, John W. Freeland, Gregory A. Fiete, and Jak Chakhalian, Nat. Commun. **4**, 2714 (2013).
[38]S Catalano, M Gibert, J Fowlie, J Íñiguez, J-M Triscone and J Kreisel, Rep. Prog. Phys. **81**, 046501 (2018).
[39]C.-T. Kuo, S.-C. Lin, G. Ghiringhellli, Y. Peng, G.M. De Luca, D. Di Castro, D. Betto, N. Brookes, M. Gehlmann, T. Wijnands, M. Huijben, J. Meyer-Ilse, E. Gullikson, J.B. Kortright, A. Vailionis, T. Gerber, G. Balestrino, L. Braicovich, C.S. Fadley, https://arxiv.org/pdf/1802.09743.pdf